Probing the basement of southern Tibet: evidence from crustal xenoliths entrained in a Miocene ultrapotassic dyke

G.H.-N. Chan, D.J. Waters, M.P. Searle, J.C. Aitchison, M.S.A. Horstwood, Q. Crowley, C.-H. Lo and J.S.-L. Chan

Journal of the Geological Society 2009; v. 166; p. 45-52
doi:10.1144/0016-76492007-145

Journal of the Geological Society, London, Vol. **166**, 2009, pp. 45–52. doi: 10.1144/0016-76492007-145.

Probing the basement of southern Tibet: evidence from crustal xenoliths entrained in a Miocene ultrapotassic dyke

G. H.-N. CHAN[1,2], D. J. WATERS[1]*, M. P. SEARLE[1], J. C. AITCHISON[3], M. S. A. HORSTWOOD[4], Q. CROWLEY[4], C.-H. LO[5] & J. S.-L. CHAN[3]

[1]*Department of Earth Sciences, Parks Road, Oxford University, Oxford OX1 3PR, UK*

[2]*SRK Consulting, 10 Richardson Street, West Perth, 6005 WA, Australia*

[3]*Department of Earth Sciences, University of Hong Kong, Hong Kong, P.R. China*

[4]*NERC Isotope Geosciences Laboratory, Keyworth, Nottingham NG12 5GG, UK*

[5]*Department of Geosciences, National Taiwan University, Taipei, Taiwan*

**Corresponding author (e-mail: dave.waters@earth.ox.ac.uk)*

Abstract: A variety of felsic and mafic granulites and ultramafic rocks occur as xenoliths within a 12.7 Ma ultrapotassic dyke intruding Xigaze flysch immediately to the north of the Yarlung–Tsangpo suture zone in southern Tibet. Garnet–clinopyroxene–plagioclase–quartz thermobarometry on mafic granulite xenoliths gives temperatures of 1130–1330 °C and pressures between 22 and 26 kbar indicating equilibration in the high-pressure and ultrahigh-temperature granulite field and defining a geotherm of *c*. 16 °C km^{-1}. Ultramafic xenoliths consist mainly of hornblende and biotite, probably of restitic crustal rather than mantle origin, and attained peak metamorphic conditions of 920–1130 °C and 17–24 kbar, whereas felsic granulites equilibrated at 870–900 °C at an inferred pressure of 17 kbar. *In situ* U–(Th)–Pb laser ablation inductively coupled plasma mass spectrometry dating of zircons shows that protoliths may include Proterozoic basement rocks, Late Cretaceous calc-alkaline tonalites of the Gangdese batholith root and/or remnants of a Neo-Tethyan oceanic arc. Certain zircons from a felsic granulite and an ultramafic xenolith have mean $^{206}Pb/^{238}U$ ages of 16.8 ± 0.9 Ma and 15.6 ± 0.6 Ma, respectively, and monazites from a micaceous xenolith yielded a mean $^{208}Pb/^{232}Th$ age of 14.4 ± 0.4 Ma. These results show that the southern Tibet basement reached a thickness of *c*. 80 km by 17–14 Ma at the latest and has remained unchanged until the present day.

Supplementary material: Mineral analyses used for pressure–temperature estimations and results of $^{40}Ar/^{30}Ar$ laser single-grain fusion experiments are available at http://www.geolsoc.org.uk/SUP18325.

The double-thickness (70–80 km) crust of southern Tibet (Owens & Zandt 1997; Schulte-Pelkum *et al*. 2005) includes the northern Tethyan Himalaya (Indian plate), Yarlung–Tsangpo suture zone and southern Lhasa terrane (Asian plate). Seismic imaging during the INDEPTH project (Nelson *et al*. 1996; Hauck *et al*. 1998) showed that the Tethyan Himalayan rocks thicken toward to the north, along with the northward underthrusting Greater Himalayan wedge. Moho depth deepens from 35 km under the southern margin of the Himalaya to *c*. 70–80 km thick beneath southern Tibet (Schulte-Pelkum *et al*. 2005). Upper mantle seismic velocities show that cold and strong upper mantle occurs beneath southern Tibet whereas hot and weak mantle occurs beneath north of *c*. 32°N near the position of the Bangong suture zone (Tilmann *et al*. 2003) (Fig. 1a).

Studies of lower crustal and upper mantle xenoliths play an important role in the understanding of the thickening history of the Tibetan plateau and have implications for models of plateau uplift and the Himalayan belt formation. Occurrences of lower crustal xenoliths have been reported in various parts of Tibet (Hacker *et al*. 2000, 2005; Ducea *et al*. 2003; Jolivet *et al*. 2003; Ding *et al*. 2007), but until now, no lower crustal xenoliths have been recovered from southern Tibet. In this paper we describe some rare lower crustal xenoliths collected from an ultrapotassic dyke intruding the Xigaze flysch immediately north of the Yarlung–Tsangpo suture zone (Fig. 1b). We infer depth of origin from thermobarometry, and age of protolith and timing of granulite-facies metamorphism of the xenoliths from U–(Th)–Pb dating of zircons and monazites. We use these data to determine the thermal state of the Lhasa terrane lower crust at the time of the xenolith recrystallization and speculate on the structural evolution of the southern Tibet lower crust.

Southern Tibet crustal xenolith samples

The NW–SE-trending xenolith-bearing dyke intrudes the Xigaze flysch, 20 km west of Ngamring in southern Tibet (29°19'50.05"N, 87°0'39.17"E; Fig. 1b). It is andesitic (SiO_2 56.1 wt%) and ultrapotassic ($K_2O/Na_2O = 7.7$; K_2O 5.7 wt%) with a high concentration of incompatible trace elements (e.g. Rb 340 ppm). Petrographically, biotite and potassium feldspar phenocrysts occur in a microcrystalline matrix of potassium feldspar, biotite, quartz, titaniferous magnetite and glass. The entrained xenoliths range in size from 5 to 100 mm, and include diopside marble, quartzite, felsic and mafic granulite, and ultramafic xenoliths. The felsic granulites consist of quartz + plagioclase + potassium feldspar + garnet + rutile + apatite + zircon ± biotite, whereas the mafic granulites comprise plagioclase + clinopyroxene + garnet + quartz + amphibole + rutile + apatite ± biotite ± zircon. The ultramafic xenoliths consist of clinopyroxene + garnet + amphibole + biotite + titanite + rutile + apatite ± plagioclase ± pyrite ± zircon. In addition, a rare

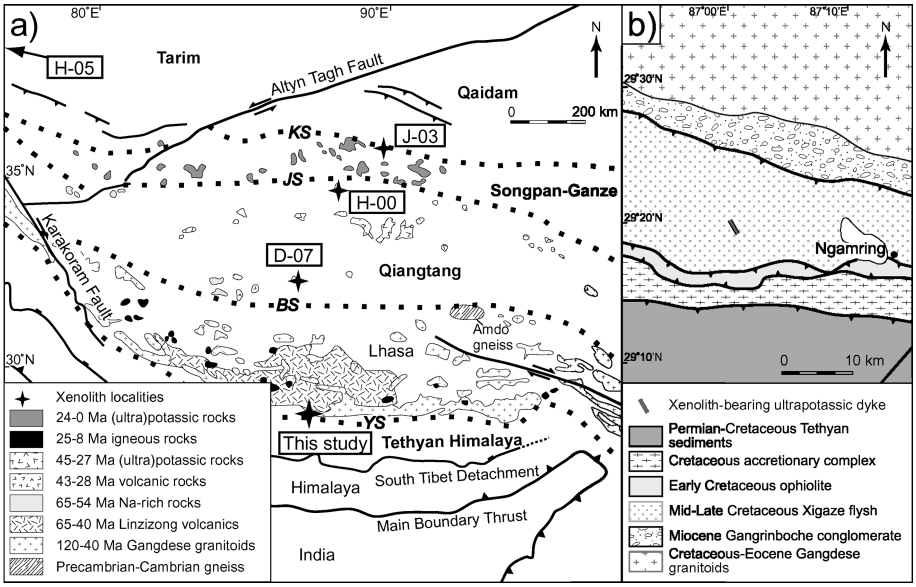

Fig. 1. (**a**) Map of the Tibetan Plateau, showing sample location, terranes, sutures, major faults and distribution of Cenozoic magmatism. YS, Yarlung–Tsangpo suture zone; BS, Bangong–Nujiang suture; JS, Jinsha suture; KS, Kunlun suture, modified after Ding *et al*. (2007); other xenolith localities: D-07, Yibuchaka (Ding *et al*. 2007); H-00, Taipinghu volcanic field (Hacker *et al*. 2000); J-03, Jingyu, Kunlun fault zone (Jolivet *et al*. 2003); H-05, arrow points towards location of Dunkeldik pipes in the Pamir range at *c*. 37°40'N, 75°E (Ducea *et al*. 2003; Hacker *et al*. 2005). (**b**) Map showing the xenolith-bearing ultrapotassic dyke cutting Xigaze flysch to the immediate north of the Yarlung–Tsangpo suture zone. Modified after Wang *et al*. (1984) and the present authors' observation.

micaceous xenolith dominated by biotite with trace amounts of garnet, rutile, apatite, zircon and monazite was also found.

All meta-igneous xenoliths are granoblastic, except for the micaceous xenolith, which is foliated. Most of the mafic granulites and ultramafic xenoliths exhibit secondary textures including the breakdown of primary sodic clinopyroxene to plagioclase + low-Na clinopyroxene symplectite and formation of kelyphite rinds tens of micrometres thick surrounding garnets. These kelyphites are interpreted to have formed during decompression in a H_2O-undersaturated environment (O'Brien & Rotzler 2003). Textures in the micaceous xenolith demonstrate that it has been extensively modified, probably during its ascent to the surface in the magma. Textures include formation of quenched melt pockets, dehydration melting of biotite to form potassium feldspar + spinel, and growth of new fine-grained biotite + potassium feldspar + quartz + apatite + titaniferous magnetite. These new phases also form the kelyphitic coronae around embayed garnets.

Mineral compositions and backscattered electron (BSE) images were acquired at Oxford University with a JEOL JXA8800R electron microprobe equipped with four wavelength spectrometers and a JEOL JSM-840A scanning electron microscope equipped with an Oxford Instruments Isis 300 energy-dispersive analytical system. Operating conditions were 10–20 s counting time on each element peak, 20 kV accelerating voltage and 40 nA beam current for the microprobe, and 100 s live counting time, 20 kV accelerating voltage and 6 nA beam current for the SEM. Both instruments were calibrated with the same set of standards and the ZAF correction procedure was used. Thermobarometry was determined using conventional thermometers (Powell 1985; Fuhrman & Lindsley 1988; Holdaway 2000) in combination with THERMOCALC 3.25 in average P mode (Powell & Holland 1988). Results for the samples and the geothermobarometers are presented in Table 1 and plotted in Figure 2. The lack of zoning and restricted occurrence of retrograde minerals at rims indicate that the major phases in the xenoliths are well equilibrated, and the rocks experienced fast cooling and decompression with rapid exhumation to the surface. Heating of the xenoliths during their entrainment in the magma is a possibility; however, the temperature estimations reported here are unlikely to reflect this transient event given the short time scales and slow rate of volume diffusion of garnet and pyroxene (Hacker *et al*. 2005). The mafic granulites have the ideal mineral assemblage of Grt + Cpx + Plag + Qtz for thermobarometry. Application of the Grt–Cpx Fe–Mg exchange thermometer (Powell 1985) coupled with THERMOCALC 3.25 in average P mode reveals that sample 158f and 158o recrystallized at conditions of 1330 ± 50 °C, 25.8 ± 1.9 kbar and 1130 ± 50 °C, 21.9 ± 0.9 kbar, respectively. Using the same combination of geothermobarometers, the ultramafic xenolith (158m) is estimated to have reached equilibrium at conditions of 920 ± 50 °C and 17.4 ± 1.0 kbar. These three samples define a linear array that corresponds to a geothermal gradient of *c*. 16°C km^{-1}. Grt–Cpx thermometry on another ultramafic xenolith (158p) yields an equilibrium temperature of 1100–1130 °C, but quantitative barometry cannot be performed on this sample as both plagioclase and quartz are absent. If all the samples are assumed to have been extracted along the same geotherm, an equilibrium pressure of 19–24 kbar can be estimated for 158p. By the same logic, the felsic granulite 158g equilibrated at 15–20 kbar with the temperature determined as 870–900 °C from coexisting ternary feldspars (Fuhrman & Lindsley 1988), whereas the micaceous xenolith records an Fe–Mg exchange temperature of 740–755 °C calculated with the Grt–Bt geothermometer of Holdaway (2000, calibration 5AV) at an assumed pressure of 13–17 kbar. Bulk-rock composition estimated by combining mineral modes from BSE image measurements with microprobe analyses (Table 2) suggests that the mafic and felsic granulites are derived from calc-alkaline tonalitic and granitic crust. The ultramafic xenoliths are rich in hornblende and biotite, have Mg-number of 43.6–48.1 and contain 15.4–27.8 % normative olivine. These features resemble those of ultramafic rocks of restitic crustal rather than mantle origin. Such rocks probably crystallized at the base of a thickened arc-crust, as discussed below (compare the Kohistan intra-oceanic arc, Yamamoto & Yoshino 1998). The micaceous xenolith consists of >95% biotite with Mg-number 67. The mineral chemistry and associations are not appropriate for a mantle-derived glimmerite, and the bulk composition does not correspond to any normal sediment. Possible origins include: a residue from wet melting of pelite; hydrothermal or K-metasomatic alteration of mafic rock; or pre-metamorphic degradation and leaching of mafic volcanic material (see Moore & Waters 1990).

Table 1. *Thermobarometry calculations*

Sample	Rock type	T (°C)	Method	P (kbar)	Method
158a	Micaceous xenolith	740–755	Grt–Bt (Holdaway 2000, calibration 5AV)	13–17	Assumed
158f	Mafic granulite	1330 ± 50	Grt–Cpx (Powell 1985)	25.8 ± 1.9	THERMOCALC, $aH_2O = 0.5$[1]
158g	Felsic granulite	870–900	Two-feldspar (Fuhrman & Lindsley 1988)	15–20	Assumed
158m	Ultramafic xenolith	920 ± 50	Grt–Cpx (Powell 1985)	17.4 ± 1.0	THERMOCALC, CaTs excluded,[2] $aH_2O = 0.5$[1]
158o	Mafic granulite	1130 ± 50	Grt–Cpx (Powell 1985)	21.9 ± 0.9	THERMOCALC, CaTs excluded[2]
158p	Ultramafic xenolith	1110–1130	Grt–Cpx (Powell 1985)	19–24	Assumed

[1]H_2O activity was set at 0.5.
[2]Calcium Tschermaks (CaTs) end-member was excluded from THERMOCALC calculation.

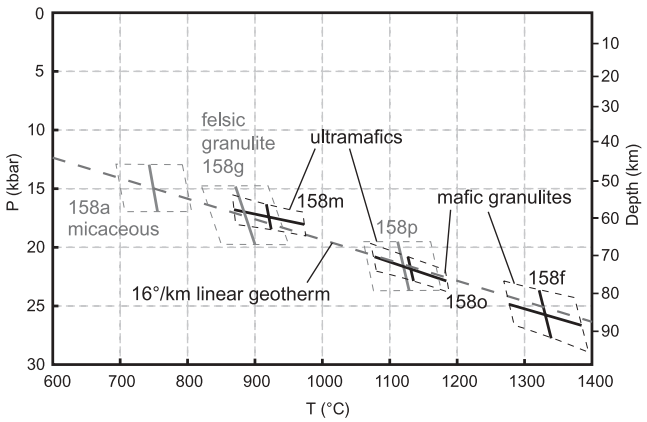

Fig. 2. Calculated thermobarometry for the studied xenoliths. Grey lines for partially constrained samples 158a, 158g and 158p, in which P–T conditions are determined by intersection between geothermometer equilibria and the linear geotherm defined by the remaining samples.

Geochronology

Biotite separates from the host dyke were dated by the $^{40}Ar/^{39}Ar$ laser single-grain fusion method at the National Taiwan University. Mineral separates were extracted from the sample by handpicking and subsequently irradiated together with the LP-6 biotite standards (Odin *et al.* 1982) in the VT-C position for 30 h at the THOR reactor. After irradiation, standards were totally fused using a double-vacuum resistant furnace and samples were incrementally heated using a US LASER Nd-YAG laser operated in a continuous mode by changing laser output energy. The gas was analysed by a VG 3600 mass spectrometer. Detailed analytical procedures have been given by Lo *et al.* (2002). The analytical results are available as Supplementary Data and are plotted on the isotope correlation diagram of $^{39}Ar/^{40}Ar$ vs $^{36}Ar/^{40}Ar$, which gives an intercept age of 12.7 ± 0.1 (1σ) Ma with mean square of weighted deviates (MSWD) = 1.6 (Fig. 3a).

In situ U–(Th)–Pb laser ablation multi-collector inductively coupled plasma mass spectrometry (MC-ICP-MS) dating of zircons and monazites in polished thin sections was performed on three of the xenoliths at the NERC Isotope Geosciences

Table 2. *Calculated bulk-rock compositions (in wt%) and normative mineral contents*

Sample:	158a	158f	158g	158m	158o	158p
Rock type:	Micaceous xenolith	Mafic granulite	Felsic granulite	Ultramafic xenolith	Mafic granulite	Ultramafic xenolith
SiO_2	37.9	57.8	74.1	45.6	66.5	43.6
TiO_2	4.8	0.3	0.0	2.0	0.1	1.7
Al_2O_3	19.0	18.0	14.3	16.9	17.3	15.4
FeO	13.5	5.3	1.4	9.4	3.4	13.9
MnO	0.1	0.0	0.0	0.1	0.1	0.2
MgO	14.8	4.4	0.6	8.7	1.8	10.8
CaO	0.2	8.8	2.2	13.2	4.9	11.4
Na_2O	0.3	4.6	3.1	2.1	4.7	1.1
K_2O	9.4	0.8	4.2	1.8	1.3	1.9
Forced sum	100.0	100.0	100.0	100.0	100.0	100.0
Mg-no.	52.3	45.3	31.4	48.1	34.7	43.6
Q	0.0	2.3	33.3	0.0	19.1	0.0
Ab	0.8	39.8	26.6	1.9	40.4	0.0
An	0.0	25.1	10.4	31.5	21.7	31.5
Or	0.0	4.9	25.0	10.4	7.5	9.8
Ne	1.6	0.0	0.0	8.6	0.0	5.1
Lc	41.9	0.0	0.0	0.0	0.0	0.9
C	8.1	0.0	0.7	0.0	0.0	0.0
Di	0.0	14.3	0.0	27.5	1.3	20.5
Hy	0.0	12.6	3.9	0.0	9.6	0.0
Ol	37.5	0.0	0.0	15.4	0.0	27.8
Il	9.2	0.5	0.1	3.8	0.2	3.3
Mt	1.1	0.4	0.1	0.8	0.3	1.1

Norm calculation assumes 5% of total Fe as Fe_2O_3.

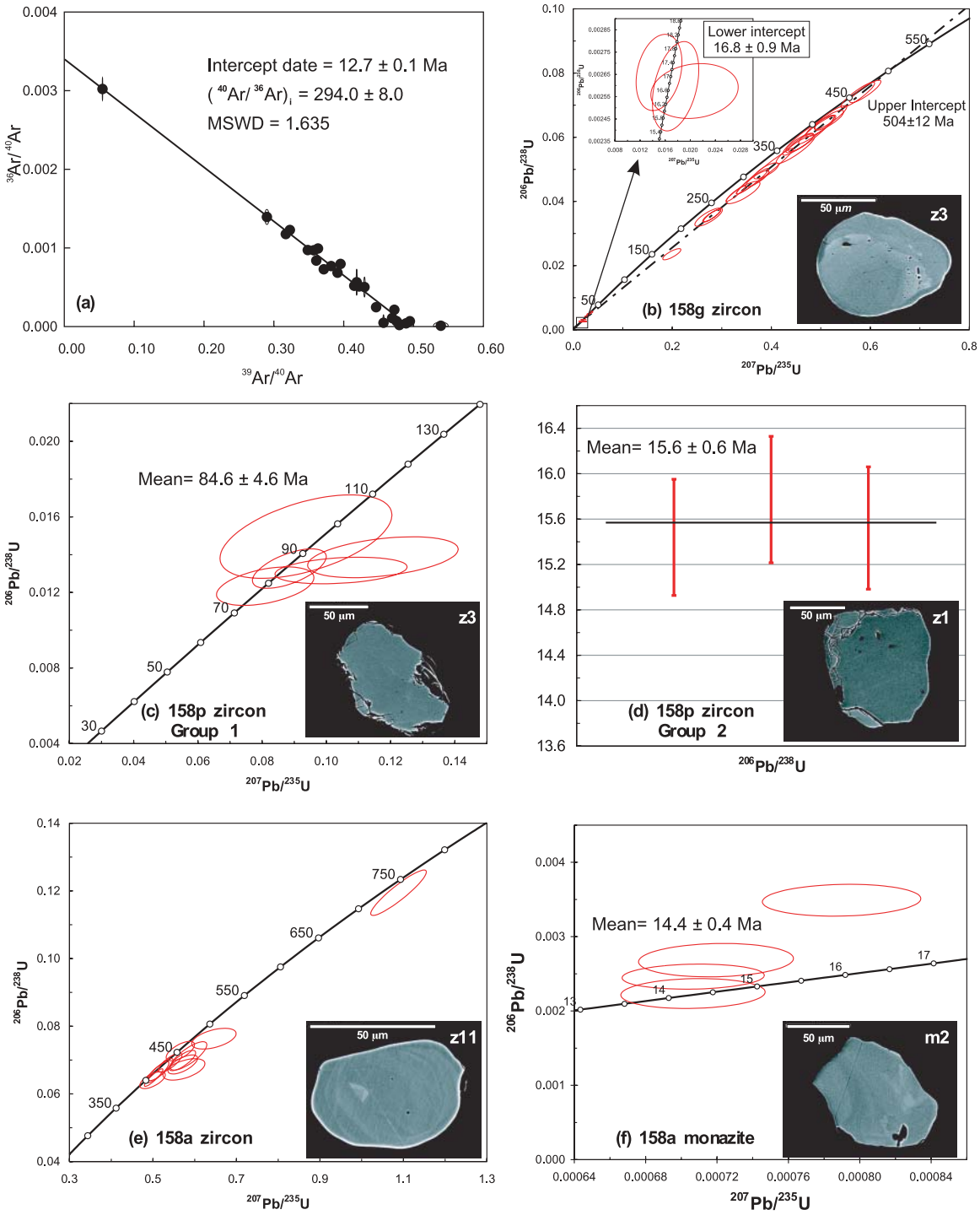

Fig. 3. (**a**) $^{36}Ar/^{40}Ar$–$^{39}Ar/^{40}Ar$ isotope correlation diagram for the biotite separates from the xenolith-bearing dyke (errors given in the figure are at 1σ); (**b**–**f**) Back-scattered electron images of representative zircon and monazite from the analysed samples (uniform scale bar represents 50 μm) and concordia diagrams (**b**, **c**, **e** and **f**) and $^{206}Pb/^{238}U$ weighted average diagram (**d**). All errors are at 2σ. Analyses include laser ablation spots in cores and at tips of single crystals.

Laboratory using Nu-Plasma HR and Thermo-Elemental Axiom MC-ICP-MS systems. The grains were ablated using a New Wave Research UP193SS Nd:YAG laser ablation system, using a spot of 20 or 35 μm diameter or a line raster 20 μm wide, depending on the size of the crystal. Measurement procedures were conducted following Horstwood *et al.* (2003), with the procedure for monazite being modified to include an additional magnet jump to allow collection of ^{232}Th. Hardware parameters for the Nu Plasma illustrating collection of U–Pb data have been described by Simonetti *et al.* (2005). The collected data were

reduced and errors propagated using an in-house spreadsheet calculation package. For zircons, each age reported here represents the weighted mean of concordant clustered $^{206}Pb/^{238}U$ ages obtained from single zircons. For monazites, owing to the presence of excess ^{206}Pb arising from *in situ* decay of ^{230}Th, only the unaffected $^{208}Pb/^{232}Th$ ages are reported here. Analytical data are plotted in Figure 3b–f and tabulated in Tables 3 and 4.

In the felsic granulite sample (GCT-158g), most data define a discordia with a 504 ± 12 (2σ) Ma upper intercept (MSWD = 1.4) (Fig. 3b). If we consider only the youngest three data points, the weighted mean $^{206}Pb/^{238}U$ age is 16.8 ± 0.9 Ma (MSWD = 0.12), and we interpret this to be the best estimate of the young end member. Together with the zoning pattern shown in the BSE images (Fig. 3b), these data are interpreted to represent a two-component mixture of Cambrian igneous (cores or entire grains) and Middle Miocene metamorphic components (mostly rims). Zircons in the ultramafic xenolith (GCT-158p) occur as inclusions or along grain boundary zones. These grains do not exhibit any zoning in their BSE images and most grains form a sub-concordant cluster of data with a weighted mean $^{206}Pb/^{238}U$ age of 84.6 ± 4.6 Ma (MSWD = 0.63) (Fig. 3c). One grain has a younger weighted mean $^{206}Pb/^{238}U$ age of 15.6 ± 0.6 Ma (MSWD = 0.10) (Fig. 3d). These ages suggest that the rock has a Late Cretaceous protolith component and experienced zircon growth during peak metamorphism in the Middle Miocene. The zircons from the micaceous xenolith (GCT-158a) are zoned. Apart from a discordant grain core with a $^{206}Pb/^{238}U$ age of 727 Ma, most data form a sub-concordant cluster around 400–474 Ma (Fig. 3e). The interpretation of the age of this rock is complex. At least two age components are inferred to exist: Proterozoic and *c*. 450 Ma, with some data points representing a mixing of these components plus Pb loss and/or zircon growth at *c*. 450 Ma and/or recently. Monazites from the same sample yield much younger ages, and three out of four analyses yielded a weighted mean age of $^{208}Pb/^{232}Th$ age of 14.4 ± 0.4 Ma with MSWD = 0.18 (Fig. 3f).

Discussion

The composition and structure of the lower crust beneath southern Tibet remain unknown, but it could comprise any of three units: (1) underthrust Indian plate lower crust, composed mainly of Early Proterozoic–Archaean granulites; (2) subducted Indian passive margin sequence and Tethyan oceanic rocks, comprising Precambrian–Cretaceous sediments and trapped remnants of Mesozoic ophiolites, island arcs; (3) thickened Lhasa terrane lower crust, consisting of presumed Precambrian basement, and Gangdese and Linzizong magmatic arc rocks. The U–Th–Pb ages obtained from this study provide new constraints on these hypotheses. The presence of *c*. 85 Ma zircons in the ultramafic xenolith demonstrates that the rocks are unlikely to be dominated by Indian plate material, in which magmatic rocks of that age are absent. In contrast, these zircon ages are comparable with the Late Cretaceous–early Palaeogene (120–49 Ma) Trans-Himalayan Gangdese magmatic arc. Moreover, recent isotopic evidence from mid-Miocene dykes emplaced south of the Yarlung–Tsangpo suture (King *et al*. 2007) indicates that Asian crust existed at depth to the south of the study area by the time of xenolith sampling. These zircon ages could also be compared with the Kohistan intra-oceanic arc in Pakistan, which contains 82–99 Ma mafic and ultramafic rocks and formed above a north-dipping intra-oceanic subduction zone of Neo-Tethys (Schaltegger *et al*. 2002). If the lower crust originated in this way, this requires part of such an arc to have been accreted during northward subduction beneath southern Tibet prior to the India–Asia collision. The *c*. 504 Ma zircons in the felsic granulites and the Late Ordovician–Early Devonian zircons with Proterozoic inheritance in the micaceous xenolith do not place any further constraints on the protolith origins, as magmatic or metamorphic rocks of these ages occur in both Indian and Asian crust. For example, Precambrian basement rocks have been recovered in Amdo along the Bangong–Nujiang suture (Guynn *et al*. 2006). Detrital zircons of similar age were found in the Great Himalaya Sequence and Tethyan succession (DeCelles *et al*. 2000). Nevertheless, our results suggest that the lower crust of the southern Lhasa terrane attained peak granulite-facies metamorphism at *c*. 17–14 Ma, slightly predating the timing of entrainment in the ultra-potassic dyke and transport to the surface.

The xenoliths can be compared with other suites sampled by volcanic rocks of different ages (0.5–28 Ma) distributed across Tibet (Fig. 1) and westward into the Pamirs, most of which also indicate a metamorphic crystallization a few million years before entrainment. The xenoliths of this study were extracted during ultrapotassic magmatism at *c*. 13 Ma from crustal levels of 50–80 km along a well-constrained geotherm of 16 °C km^{-1}. By 13 Ma, therefore, part of the lower crust of the southern Lhasa terrane was represented by hot and dry tonalitic mafic and felsic granulites and ultramafic rocks, perhaps with a minor component of supracrustal material. The xenolith suite described from 28 Ma Na-rich calc-alkaline lavas in the southern Qiangtang terrane by Ding *et al*. (2007) is similarly dominated by meta-igneous mafic granulites, although these appear to define a hotter geotherm passing through *c*. 980 °C at a maximum depth of around 45 km. In the Pamir, 11 Ma ultrapotassic lavas intruding the southern margin of the westernmost Qiangtang terrane (Ducea *et al*. 2003; Hacker *et al*. 2005) contain a suite of meta-igneous eclogitic and granulitic xenoliths that recrystallized mainly at conditions of 1000–1100 °C and 23–28 kbar, on a cooler geotherm of 10–12 °C km^{-1}. In contrast, however, a suite of xenoliths described from a 3 Ma ultrapotassic dyke in the northern Qiangtang terrane of north–central Tibet (Hacker *et al*. 2000) show that the lower crust there is occupied by anhydrous meta-sedimentary granulite-facies rocks that equilibrated at 800–1100 °C on a hot geotherm at depths of 30–50 km (Hacker *et al*. 2000). Still further north, mafic granulitic xenoliths that attained peak metamorphic conditions of 1000–1100 °C at depths of 50–60 km have also been recovered from 0.5 Ma shoshonitic lavas in the northern Songpan–Ganze terrane (Jolivet *et al*. 2003). In summary, the xenoliths of southern Tibet coupled with other lower crustal xenolith information described above support a two-part crustal structure model for Tibet and the Pamir (Schwab *et al*. 2004; Hacker *et al*. 2005). A crystalline basement extends from the southern Lhasa terrane to the southern Qiantang terrane, with a possible western extension to the Pamir. Beyond this zone, the lower crust is occupied mainly by meta-sedimentary rocks at least to the northern Qiangtang terrane.

The southern margin of the Asian plate is dominated by an extensive calc-alkaline batholith: the Gangdese granitoids with associated subaerial andesitic extrusive rocks (Linzizong Formation). A major regional unconformity across southern Tibet has been documented, with gently dipping Palaeocene Linzizong volcanic rocks above folded mid- to late Cretaceous Takena Formation red-beds, showing that significant crustal thickening occurred prior to the India–Asia collision (England & Searle 1986; Kapp *et al*. 2007; Leier *et al*. 2007). Given the geology of southern Tibet, it is likely that the southern margin of Asia was similar to an Andean-type margin, both in crustal thickness and elevation, during that time. The exact thickness of the crust of

Table 3. *LA-MC-ICPMS zircon data*

Sample	Analysis	^{204}Pb (mV)	^{206}Pb (mV)	^{207}Pb (mV)	^{238}U (mV)	U (ppm)[1]	Isotopic ratios[2]							Ages (Ma)					
							^{207}Pb/^{206}Pb	2σ %	^{206}Pb/^{238}U	2σ %	^{207}Pb/^{235}U	2σ %	Rho	^{207}Pb/^{206}Pb	2σ	^{206}Pb/^{238}U	2σ	^{207}Pb/^{235}U	2σ
Sample 158a																			
z11-1	Core	n.a.	6.86	0.39	65	434	0.0661	2.0	0.1195	4.6	1.0884	5.0	0.92	809.1	41.7	727.4	35.3	747.7	53.9
z11-2	Rim	0.000	3.19	0.17	55	371	0.0620	6.0	0.0672	3.9	0.5743	7.2	0.54	672.4	129.0	419.5	16.7	460.8	40.9
z17-1	Rim	n.a.	2.52	0.13	41	277	0.0603	3.8	0.0687	3.3	0.5713	5.1	0.66	615.1	82.3	428.3	14.8	458.9	29.0
z17-2	Rim	n.a.	14.57	0.71	256	1713	0.0561	1.6	0.0648	3.3	0.5016	3.6	0.90	457.5	34.5	404.8	13.7	412.8	18.3
z17-3	Core	n.a.	2.41	0.13	36	239	0.0614	5.9	0.0763	3.3	0.6461	6.7	0.49	653.3	126.0	474.1	16.1	506.1	43.2
z16-1c	Rim	n.a.	6.00	0.29	99	666	0.0560	2.3	0.0672	4.0	0.5190	4.6	0.86	453.4	51.6	419.1	17.2	424.5	24.0
z16-2	Rim	n.a.	5.70	0.28	94	627	0.0567	2.6	0.0692	3.4	0.5413	4.3	0.79	479.6	57.9	431.6	15.0	439.3	23.2
z16-3c	Rim	n.a.	6.15	0.30	104	696	0.0558	2.3	0.0664	3.9	0.5103	4.5	0.86	442.9	51.2	414.3	16.5	418.6	23.1
z15-1	Core	n.a.	2.48	0.12	44	296	0.0565	3.9	0.0641	3.2	0.4989	5.0	0.63	471.3	85.9	400.3	13.1	411.0	25.1
z15-3	Rim	n.a.	2.72	0.14	43	287	0.0565	3.7	0.0726	3.2	0.5656	4.9	0.66	470.6	82.2	452.1	15.1	455.1	27.9
Sample 158g																			
z2-1b	Rim	n.a.	1.64	0.08	49	327	0.0565	5.0	0.0351	6.6	0.2735	8.3	0.80	472.9	111.2	222.4	15.0	245.5	22.9
z2-1c	Core	0.007	3.52	0.17	59	396	0.0568	3.2	0.0606	8.4	0.4749	9.0	0.93	485.2	70.4	379.3	32.6	394.6	42.3
z3-1b	Core	n.a.	3.47	0.17	72	483	0.0571	3.2	0.0495	4.2	0.3898	5.2	0.79	494.7	70.7	311.6	13.2	334.2	20.6
z3-1c	Core	0.005	1.87	0.09	46	306	0.0582	4.8	0.0428	6.6	0.3431	8.1	0.81	536.1	104.0	270.1	18.2	299.5	28.0
z3-2b	Rim	n.a.	3.40	0.18	151	1015	0.0613	4.5	0.0236	6.0	0.1992	7.5	0.80	651.2	95.7	150.1	9.2	184.4	15.1
z3-2c	Rim	0.002	4.58	0.22	133	893	0.0570	2.7	0.0355	4.5	0.2791	5.2	0.86	492.2	59.0	224.9	10.3	250.0	14.7
z3-3b	Rim	n.a.	5.48	0.26	162	1084	0.0571	2.4	0.0357	4.5	0.2809	5.1	0.88	495.6	53.8	226.0	10.3	251.4	14.5
z3-3c	Rim	n.a.	5.88	0.28	135	908	0.0567	2.3	0.0463	7.0	0.3620	7.4	0.95	479.8	51.6	291.8	20.8	313.7	26.7
z5-1b	Rim	0.000	0.25	0.01	88	589	0.0493	15.9	0.0026	6.3	0.0177	17.1	0.37	162.7	371.2	16.7	1.1	17.8	3.1
z5-2a	Core	0.000	0.62	0.02	150	1007	0.0474	10.5	0.0042	5.9	0.0272	12.0	0.49	69.1	249.4	26.8	1.6	27.2	3.3
z6-2c	Homogeneous	0.004	0.25	0.01	86	579	0.0410	19.2	0.0027	5.3	0.0150	19.9	0.26	−290.0	489.0	17.1	0.9	15.1	3.0
z6-4b	Homogeneous	0.007	0.18	0.01	65	435	0.0582	27.2	0.0026	3.9	0.0207	27.5	0.14	538.3	595.8	16.6	0.6	20.8	5.8
z7-1b	Core	0.000	5.43	0.26	78	525	0.0571	2.5	0.0635	4.3	0.5000	5.0	0.87	494.5	54.5	397.1	17.7	411.7	25.0
z7-1c	Core	n.a.	7.56	0.36	94	630	0.0569	2.0	0.0732	4.4	0.5747	4.8	0.91	488.9	44.1	455.5	20.8	461.0	27.9
z7-2	Rim	0.001	4.61	0.22	90	600	0.0568	2.7	0.0494	11.9	0.3872	12.2	0.98	485.3	59.3	310.9	37.7	332.3	46.7
z7-3	Rim	0.001	4.46	0.22	89	598	0.0573	2.7	0.0471	4.4	0.3720	5.2	0.85	501.8	59.9	296.8	13.3	321.1	19.3
z7-4b	Core	n.a.	7.72	0.37	113	759	0.0572	2.0	0.0623	5.7	0.4915	6.1	0.94	498.9	44.8	389.8	22.9	406.0	29.8
z7-4c	Core	n.a.	7.37	0.36	90	606	0.0576	2.1	0.0743	3.9	0.5899	4.4	0.88	514.9	45.2	461.8	18.4	470.8	25.8
z8-1	Core	n.a.	5.67	0.27	78	526	0.0570	2.4	0.0662	4.6	0.5198	5.1	0.89	490.1	52.2	413.1	19.5	425.0	26.8
z8-2c	Core	n.a.	5.73	0.28	90	600	0.0573	2.4	0.0582	3.8	0.4598	4.5	0.85	501.5	52.2	365.0	14.4	384.1	20.8
z8-3	Core	0.002	5.12	0.25	71	475	0.0574	2.5	0.0653	3.9	0.5168	4.6	0.84	507.4	55.5	407.7	16.4	423.0	24.1
z8-4	Rim	0.002	3.62	0.18	59	393	0.0579	3.1	0.0562	6.4	0.4489	7.1	0.90	526.3	67.3	352.6	23.1	376.5	31.8
z8-5b	Rim	0.002	4.49	0.22	72	483	0.0570	2.8	0.0582	4.3	0.4576	5.1	0.84	491.5	61.0	364.8	15.9	382.6	23.3
z9-1c	Core	n.a.	0.23	0.01	76	509	0.0479	19.7	0.0032	1.9	0.0209	19.8	0.09	93.7	467.3	20.4	0.4	21.0	4.2
z10-1	Core	n.a.	10.83	0.51	236	1582	0.0561	1.7	0.0424	4.7	0.3283	5.0	0.94	457.4	36.8	267.8	12.8	288.3	16.4
z10-2	Rim	n.a.	1.22	0.05	209	1398	0.0483	6.5	0.0054	4.8	0.0361	8.1	0.60	112.2	153.0	34.9	1.7	36.0	3.0
z10-3	Rim	n.a.	1.12	0.04	208	1396	0.0457	7.2	0.0049	4.0	0.0311	8.2	0.48	−17.6	173.5	31.7	1.3	31.1	2.6
Sample 158p																			
z1-1b	Homogeneous	n.a.	0.04	0.00	23	140	n.a.	n.a.	0.0024	3.3	n.a.	n.a.	n.a.	n.a.	n.a.	15.4	0.5	n.a.	n.a.
z1-2b	Homogeneous	n.a.	0.05	0.00	25	152	n.a.	n.a.	0.0024	3.5	n.a.	n.a.	n.a.	n.a.	n.a.	15.8	0.6	n.a.	n.a.
z1-3b	Homogeneous	n.a.	0.06	0.00	33	203	n.a.	n.a.	0.0024	3.5	n.a.	n.a.	n.a.	n.a.	n.a.	15.5	0.5	n.a.	n.a.
z3-1b	Homogeneous	n.a.	0.26	0.01	26	157	0.0576	15.5	0.0132	4.4	0.1046	16.1	0.27	515.8	340.1	84.3	3.7	101.0	16.9
z5-1c	Homogeneous	n.a.	0.23	0.01	20	124	0.0615	15.0	0.0139	6.4	0.1176	16.3	0.39	657.7	321.7	88.8	5.7	112.9	19.3
z7-1b	Core	0.000	0.35	0.01	34	207	0.0476	13.8	0.0123	6.8	0.0810	15.3	0.44	80.2	326.5	79.0	5.4	79.1	12.5
z7-2b	Core	0.001	0.78	0.03	71	434	0.0484	8.5	0.0133	6.4	0.0885	10.6	0.61	118.3	199.2	84.9	5.5	86.1	9.5
z6-2a	Homogeneous	0.001	0.19	0.01	16	97	0.0454	20.0	0.0150	12.1	0.0937	23.3	0.52	−33.1	484.6	95.7	11.6	90.9	22.0

[1]Accuracy of U content is *c.* 20%.
[2]All isotopic ratios are not common-Pb corrected.
Homogeneous inducates structureless zircon, with no zoning. n.a., not available.

Table 4. *LA-MC-ICPMS monazite data*

Sample	Analysis	^{204}Pb (mV)	^{206}Pb (mV)	^{208}Pb (mV)	^{232}Th (mV)	^{238}U (mV)	Th[1] (ppm)	Th/U[2]	Common-Pb corrected isotopic ratios						Common-Pb corrected ages[4] (Ma)			
									f206[3] %	^{206}Pb/^{238}U	2σ %	^{208}Pb/^{232}Th	2σ %		^{206}Pb/^{238}U	2σ	^{208}Pb/^{232}Th	2σ
Sample 158a																		
m10_1	Core	0.006	1.5	10.1	2546.92	184.69	38939	25.4	6.71	0.0035	5.0	0.000790	4.6		22.5	1.1	16.0	0.7
m2_1	Rim	0.011	1.4	9.5	2731.45	239.26	41760	21.0	12.45	0.0022	7.3	0.000707	4.7		14.4	1.1	14.3	0.7
m3_1	Rim	0.008	1.7	10.8	3104.35	299.71	47462	19.0	8.41	0.0027	6.8	0.000719	4.9		17.3	1.2	14.5	0.7
m4_1	Rim	0.008	1.8	10.8	3157.30	340.61	48271	17.0	7.90	0.0025	5.6	0.000707	4.6		15.9	0.9	14.3	0.7

[1]Accuracy of Th content is *c*. 20%.
[2]Normalized to Th/U ratio of the standard.
[3]Common ^{206}Pb expressed as a percentage of total ^{206}Pb measured.
[4]Isotopic ratios are corrected for common-Pb. Common-Pb correction based on a two-stage model (Stacey and Kramers 1975) and the interpreted age of the crystal.

the margin by the time of collision is unclear, but could be around 60 km. This suggests that the basement of the southern Lhasa terrane thickened from 60 km in the Eocene only to 75–80 km by *c*. 17–14 Ma and has remained unchanged until the present day. By corollary, the thickened basement could have allowed the southern Lhasa terrane to reach its present elevation by *c*. 17–14 Ma, consistent with other palaeoaltimetry estimates (Spicer *et al*. 2003; Rowley & Currie 2006). The xenolith temperature estimations indicate that a geothermal gradient of 16 °C km^{-1} prevailed at *c*. 17-14 Ma. This elevated geothermal gradient, together with the widespread occurrence of ultrapotassic and adakitic volcanic rocks in southern Tibet (e.g. Chung *et al*. 2005), indicates that the ambient temperature of the lower crust and upper mantle experienced a major thermal perturbation. Models for convective removal of thickened lithospheric mantle (England & Houseman 1986; Turner *et al*. 1993), slab break-off (Maheo *et al*. 2002) and intracontinental subduction (Arnaud *et al*. 1992) could potentially explain the heat advection in the mantle. All these models emphasize the importance of heating from the underlying asthenosphere. Alternatively, the xenolith geotherm, which is less extreme than that recorded by xenolith suites further north, may reflect the culmination of crustal thickening in the southern Lhasa terrane by that time, in which case the heat may have been derived from crustal radioactivity without input from the underlying mantle lithosphere (McKenzie & Priestley 2008).

We thank V. Pashley, N. Charnley and P. Jackson for sample preparation and analysis. G.H.-N.C. has been funded by a Croucher Foundation Scholarship. This work was supported by HKU CRCG and the Research Grants Council of the Hong Kong Special Administrative Region, China (HKU 7001/04P) to J. Aitchison. Isotope work at NIGL was funded by NERC (NIGFSC project 20427). The earliest version of the manuscript benefited from the comments of S. Harley, B. Hacker and L. Ratschbacher. T. Argles and an anonymous reviewer are thanked for their insightful comments.

References

Arnaud, N.O., Vidal, P., Tapponnier, P., Matte, P. & Deng, W.M. 1992. The high K_2O volcanism of northwestern Tibet: geochemistry and tectonic implications. *Earth and Planetary Science Letters*, **111**, 351–367.

Chung, S.-L., Chu, M.-F., Zhang, Y., *et al*. 2005. Tibetan tectonic evolution inferred from spatial and temporal variations in post-collisional magmatism. *Earth-Science Reviews*, **68**, 173-196.

DeCelles, P.G., Gehrels, G.E., Quade, J., LaReau, B. & Spurlin, M. 2000. Tectonic implications of U/Pb zircon ages of the Himalayan orogenic belt in Nepal. *Science*, **288**, 497–499.

Ding, L., Kapp, P., Yue, Y. & Lai, Q. 2007. Postcollisional calc-alkaline lavas and xenoliths from the southern Qiangtang terrane, central Tibet. *Earth and Planetary Science Letters*, **254**, 28–38.

Ducea, M. N., Lutkov, V., Minaev, V. T., *et al*. 2003. Building the Pamirs: The view from the underside. *Geology*, **31**, 849–852.

England, P. & Houseman, G. 1986. Finite strain calculations of continental deformation: 2. Comparison with the India–Asia collision zone. *Journal of Geophysical Research*, **91**, 3664–3676.

England, P. & Searle, M.P. 1986. The Cretaceous–Tertiary deformation of the Lhasa block and its implications for the crustal thickening in Tibet. *Tectonics*, **5**, 1–14.

Fuhrman, M.L. & Lindsley, D.H. 1988. Ternary-feldspar modeling and thermometry. *American Mineralogist*, **73**, 201–215.

Guynn, H., Kapp, P.A., Heizler, M., Gehrels, G. & Ding, L. 2006. Tibetan basement rocks near Amdo reveal 'missing' Mesozoic tectonism along the Bangong suture, central Tibet. *Geology*, **34**, 505–508.

Hacker, B., Gnos, E., Ratschbacher, L., *et al*. 2000. Hot and dry deep crustal xenoliths from Tibet. *Science*, **287**, 2463–2466.

Hacker, B., Luffi, R., Lutkov, V., *et al*. 2005. Near-ultrahigh pressure processing of continental crust: Miocene crustal xenoliths from the Pamir. *Journal of Petrology*, **46**, 1661–1687.

Hauck, M.L., Nelson, K.D., Brown, L.D., Zhao, W. & Ross, A.R. 1998. Crustal

structure of the Himalayan orogen at ~90° east longitude from Project INDEPTH deep reflection profiles. *Tectonics*, **17**, 481–500.

Holdaway, M. J. 2000. Application of new experimental and garnet Margules data to the garnet–biotite thermometer. *American Mineralogist*, **85**, 881–892.

Horstwood, M.S.A., Foster, G.I., Parrish, R.R., Noble, S.R. & Nowell, G.M. 2003. Common-Pb corrected in-situ U–Pb accessory mineral geochronology by LA-MC-ICP-MS. *Journal of Analytical Atomic Spectrometry*, **18**, 837–846.

Jolivet, M., Brunel, M., Seward, D., *et al.* 2003. Neogene extension and volcanism in the Kunlun Fault Zone, northern Tibet: New constraints on the age of the Kunlun Fault. *Tectonics*, **22**, 1052.

Kapp, P., DeCelles, P.G., Leier, A.L., *et al.* 2007. The Gangdese retroarc thrust belt revealed. *GSA Today*, **17**, 4–9.

King, J., Harris, N., Argles, T., *et al.* 2007. First field evidence of southward ductile flow of Asian crust beneath southern Tibet. *Geology*, **35**, 727–730.

Leier, A. L., DeCelles, P.G., Kapp, P. & Ling, D.. 2007. The Takena Formation of the Lhasa terrane, southern Tibet: The record of a Late Cretaceous retroarc foreland basin. *Geological Society of America Bulletin*, **119**, 31–48.

Lo, C.-H., Chung, S.-L., Lee, T.-Y. & Wu, G.-Y. 2002. Age of the Emeishan flood magmatism and relations to Permian–Triassic boundary events. *Earth and Planetary Science Letters*, **198**, 449–458.

Maheo, G., Gullot, S., Blichert-Toft, J., Rolland, Y. & Pecher, A. 2002. A slab breakoff model for the Neogene thermal evolution of Southern Karakoram and South Tibet. *Earth and Planetary Science Letters*, **195**, 45–58.

McKenzie, D. & Priestley, K. 2008. The influence of lithospheric thickness variations on continental evolution. *Lithos*, **102**, 1–11.

Moore, J. M. & Waters, D. J. 1990. Geochemistry and origin of cordierite–orthoamphibole/orthopyroxene–phlogopite rocks from Namaqualand, South Africa. *Chemical Geology*, **85**, 77–100.

Nelson, K.D., Zhao, W., Brown, L.D., *et al.* 1996. Partially molten middle crust beneath southern Tibet: synthesis of project INDEPTH results. *Science*, **274**, 1684–1695.

O'Brien, P.J. & Rotzler, J. 2003. High-pressure granulites: formation, recovery of peak conditions and implications for tectonics. *Journal of Metamorphic Geology*, **21**, 3–20.

Odin, G.S., Adams, C.J., Armstrong, R.L. *et al.* 1982. Interlaboratory standards for dating purposes, *In:* Odin, G.S. (ed.) *Numerical Dating in Stratigraphy.* Wiley, Chichester, 123–149.

Owens, T.J. & Zandt, G. 1997. Implications of crustal property variations for models of Tibetan plateau evolution. *Nature*, **387**, 37–43.

Powell, R. 1985. Regression diagnostics and robust regression in geothermometer/geobarometer calibration: The garnet–clinopyroxene thermometer revisited. *Journal of Metamorphic Geology*, **3**, 327–342.

Powell, R. & Holland, T.J.B. 1988. An internally consistent dataset with uncertainties and correlations: Applications to geobarometry, worked examples and a computer program. *Journal of Metamorphic Geology*, **6**, 173–204.

Rowley, D.B. & Currie, B.S. 2006. Palaeo-altimetry of the late Eocene to Miocene Lunpola basin, central Tibet. *Nature*, **439**, 677–681.

Schaltegger, U., Zeilinger, G., Frank, M. & Burg, J.-P. 2002. Multiple mantle sources during island arc magmatism: U–Pb and Hf isotopic evidence from the Kohistan arc complex, Pakistan. *Terra Nova*, **14**, 461–468.

Schulte-Pelkum, V., Monsalve, G., Sheehan, A., Pandey, M.R., Sapkota, S., Bilham, R. & Wu, F. 2005. Imaging the Indian subcontinent beneath the Himalaya. *Nature*, **435**, 1222–1225.

Schwab, M., Ratschbacher, L., Siebel, W., *et al.* 2004. Assemblage of the Pamirs: Age and origin of magmatic belts from the southern Tien Shan to the southern Pamirs and their relation to Tibet. *Tectonics*, **23**, paper number TC4002.

Simonetti, A., Heaman, L.M., Hartlaub, R.P., Creaser, R.A., MacHattie, T.G. & Bohm, C. 2005. U–Pb zircon dating by laser ablation-MC-ICP-MS using a new multiple ion counting Faraday collector array. *Journal of Analytical Atomic Spectrometry*, **20**, 677–686.

Spicer, R. A., Harris, N. B. W., Widdowson, M., *et al.* 2003. Constant elevation of southern Tibet over the past 15 million years. *Nature*, **421**, 622–624.

Stacey, J.S. & Kramers, J.D. 1975. Approximation of terrestrial lead isotope evolution by a two-stage model. *Earth and Planetary Science Letters*, **26**, 207–221.

Tilmann, F.J., Ni, J. & INDEPTH III Seismic Team 2003. Seismic imaging of the downwelling Indian lithosphere beneath Central Tibet. *Science*, **300**, 1424–1427.

Turner, S., Hawkesworth, C., Liu, J., Rogers, N., Kelley, S. & Van Calsteren, P. 1993. Timing of Tibetan uplift constrained by analysis of volcanic rocks. *Nature*, **364**, 50–53.

Wang, X.B., Xiao, X.C., Cao, Y.G. & Zheng, H.X. 1984. *Geological map of the ophiolite zone along the middle Yarlung Zangbo (Tsangpo River), Xizang (Tibet)*. Academy of the Geological Sciences, Beijing.

Yamamoto, H. & Yoshino, T. 1998. Superposition of replacements in the mafic granulites of the Jijal complex of the Kohistan arc, northern Pakistan: dehydration and rehydration within deep arc crust. *Lithos*, **43**, 219–234.

Received 8 October 2007; revised typescript accepted 14 July 2008.
Scientific editing by Alan Collins.